Dalton Transactions

ROYAL SOCIETY OF CHEMISTRY

PAPER

View Article Online
View Journal | View Issue

Cite this: *Dalton Trans.*, 2026, **55**, 2893

A multifunctional reconfigurable terahertz chiral metasurface based on VO_2 and graphene

Hongrun Xu[a] and Zhen Cui *[a,b]

Received 1st January 2026,
Accepted 28th January 2026

DOI: 10.1039/d6dt00001k

rsc.li/dalton

Despite advancements in high integration and miniaturization, terahertz (THz) devices still face challenges such as limited functionality, tunability, and narrow application ranges. To resolve the above concerns, we present a multifunctional reconfigurable THz chiral metasurface based on vanadium dioxide (VO_2) and graphene. This structure exploits VO_2's phase transition and graphene's electrical tunability, enabling multifunctional responses. The metasurface exhibits a triple-band circular dichroism (CD) response within 1.0–3.5 THz, with peaks at 1.62 THz, 2.89 THz, and 3.19 THz, reaching values of 0.944, 0.83, and 0.88, respectively. Dynamic switching of CD peak numbers is achieved through the synergistic control of VO_2 and graphene. Under linearly polarized light incidence, the metasurface shows a single-band linear dichroism (LD) response in the 4.0–4.2 THz range, with a peak value of 0.9 at 4.093 THz. The intensity of the LD response can be reversibly tuned by adjusting the Fermi level of graphene and the incident polarization angle. Additionally, the metasurface efficiently converts polarization under both *x*-polarized and left-handed circularly polarized light. This multifunctional metasurface offers new opportunities for THz applications, such as CD supermirrors, intelligent switches, chiral photodetectors, and polarization digital imaging systems.

1. Introduction

Owing to the fast advancement of terahertz (THz) technology and nanofabrication techniques, THz metamaterials have become a frontier in optical research due to their unique ability to control electromagnetic wave propagation.[1–4] THz waves, which lie between the microwave and infrared bands (0.1–10 THz), possess both penetrability and non-ionizing properties, making them highly promising for applications in medical imaging, wireless communication, sensing, and detection.[5–9] However, due to the weak response of natural materials in the THz range, efficient manipulation of THz waves remains a challenge. The introduction of metamaterials has provided a novel approach to overcoming this bottleneck.[10,11] The core concept of metamaterials lies in designing subwavelength artificial structural units that allow flexible manipulation of the amplitude, phase, and polarization characteristics of electromagnetic waves. Furthermore, as research advanced, scientists extended the three-dimensional structures of metamaterials to two-dimensional planes, leading to the formation of ultrathin metasurfaces.[12–14]

Chirality, as one of the important characteristics in metamaterials and metasurfaces, refers to a geometric structure that cannot coincide with its mirror image through translation or rotation.[15] Since Lord Kelvin proposed the notion of chirality in 1893, the optical responses of chiral systems have gradually become a significant focus in optical research. Compared to natural chiral materials, artificial chiral metamaterials offer stronger electromagnetic responses and greater designability, enabling unique electromagnetic properties such as dichroism and polarization conversion between various polarization states.[16–18] Particularly in the THz range, chiral metasurfaces are widely applied in fields such as optical communication, polarization imaging, sensing, and absorber design, due to their excellent polarization-selective characteristics.[19–21] Dichroism is an important physical quantity that characterizes chiral metasurfaces, referring to the ability of a structure to absorb incident waves with different polarization states differently.[22,23] Based on the polarization form of the incident wave, dichroism can be classified into circular dichroism (CD) and linear dichroism (LD). CD reflects the structure's ability to differentiate the absorption of left-handed circularly polarized (LCP) light and right-handed circularly polarized (RCP) light. LD characterizes the differential response of a structure to two orthogonal linearly polarized incident waves, such as *x*- and *y*-polarized light. Under normal incidence, these polarization states are equivalent to transverse electric (TE) and transverse magnetic (TM) polarizations. In addition to selective absorp-

[a]*School of Automation and Information Engineering, Xi'an University of Technology, Xi'an, 710048, P.R. China. E-mail: zcui@xaut.edu.cn*
[b]*Xi'an Key Laboratory of Wireless Optical Communication and Network Research, Xi'an University of Technology, Xi'an, 710048, P.R. China*

tion of different polarization states, chiral metasurfaces can also achieve efficient conversion between various polarization modes, such as linear-to-linear, linear-to-circular, and circular-to-circular, through clever structural design. This further expands their application potential in polarization control and terahertz photonic devices.[24]

However, traditional chiral metasurfaces typically use metallic structures, and once their electromagnetic response is determined, it is difficult to adjust, thus limiting their application in multifunctional photonic devices. To overcome this challenge, researchers have introduced various tunable materials, such as vanadium dioxide (VO_2), graphene, photosensitive silicon, and liquid crystals.[25–28] These materials can alter their conductivity or dielectric constant through mechanisms such as thermal modulation, applied electric fields, optical excitation, or mechanical strain, thereby enabling tunability of device performance. Among these materials, VO_2 has been extensively studied for its distinctive metal–insulator phase transition behavior.[29,30] At a temperature of approximately 340 K, a reversible phase transition occurs in VO_2 between its metallic and insulating states, with its conductivity varying by about 4–5 orders of magnitude. Graphene, a typical two-dimensional material, exhibits remarkable optoelectronic properties.[31,32] Its chemical potential can be tuned *via* the application of a bias voltage or chemical doping, thereby altering the surface carrier concentration and enabling controlled modulation of its conductivity. Unlike the large discrete modulation observed in VO_2, graphene allows for small, continuous adjustments to device performance. Based on these characteristics, both VO_2 and graphene, whether used individually or in synergistic integration, show tremendous potential in the design of multifunctional reconfigurable optoelectronic devices.

In the past several years, notable progress has been achieved in the research of multifunctional reconfigurable metasurfaces, particularly those based on dynamic control structures of VO_2 and graphene, which have received widespread attention. As an illustration, Liu *et al.*33 designed a VO_2-based ultrawideband and multiband switchable terahertz metasurface, which switches between ultrawideband and multiband absorption functions by controlling the conductivity of VO_2 through temperature. Wang *et al.*34 proposed a terahertz broadband chiral metasurface constructed from a VO_2–metal hybrid configuration, where the switching and tuning of the CD response are achieved by modulating the conductivity of VO_2, with stability at wide incident angles. Zhu *et al.*[35] designed a terahertz metasurface containing both graphene and VO_2, achieving dual-frequency and broadband absorption switching through the phase transition of VO_2 and the chemical potential modulation of graphene. Yang *et al.*36 designed a chiral metasurface containing misaligned double U-shaped gold rings and graphene, achieving strong CD and perfect absorption of linearly polarized (LP) light by modulating the structural parameters and the chemical potential of graphene, with stability at wide incident angles. However, despite significant progress in the research of multifunctional reconfigurable metasurfaces in recent years, most studies remain focused on dual-functional or limitedly tunable structures, which often suffer from issues such as limited functionality, single modulation methods, low efficiency, and structural complexity. Therefore, this study aims to design a high-performance, simple-structured multifunctional reconfigurable metasurface, contributing to the advancement of terahertz optoelectronic devices.

To overcome these challenges, this paper innovatively presents a multifunctional reconfigurable terahertz chiral metasurface constructed from VO_2 and graphene. The design effectively utilizes the phase transition characteristics of VO_2 and the electrically tunable properties of graphene, enabling dynamic control of multiple functions, including triple-band switchable CD response, single-band reversible LD response, and efficient polarization conversion. In comparison with the majority of multifunctional devices reported to date, this design achieves efficient function switching through the synergistic control of VO_2 and graphene, promoting the further development of high integration and miniaturization of terahertz photonic devices.

2. Structural design and experimental methods

Through reasonable structural design and material combinations, this work achieves multiple functions from a single topological structure. In this study, by combining the reversible phase transition properties of VO_2 with the electrically tunable characteristics of graphene, the device can realize multiple operating states within the same topological structure. The functional schematic is shown in Fig. 1(d)–(f).

As shown in Fig. 1(a)–(c), the proposed multifunctional terahertz chiral metasurface consists of five layers, from bottom to top: a copper reflective bottom layer, a first dielectric layer, a graphene ring layer, a second dielectric layer, and an asymmetric composite resonant layer composed of VO_2 and copper. The bottom copper film acts as the reflective layer and can effectively block the transmission of incident terahertz waves. The top resonant layer adopts an asymmetric double J-shaped composite opening structure, consisting of two identical J-shaped copper elements and a small VO_2 patch. The VO_2 patch is located on the left side of the upper J-shaped copper element, introducing structural asymmetry to enhance the chiral response of the metasurface. Both dielectric layers are made of SiO_2, ensuring effective coupling between the graphene ring and the top resonant structure. The central graphene ring is electrically tunable *via* modulation of its chemical potential using an external voltage, while the VO_2 patch can be thermally controlled by the temperature-induced metal–insulator phase transition. Fig. 1(b) and (c) illustrate the unit structure schematic and parameter distribution of the device, and the optimized structural parameters are summarized in Table 1.

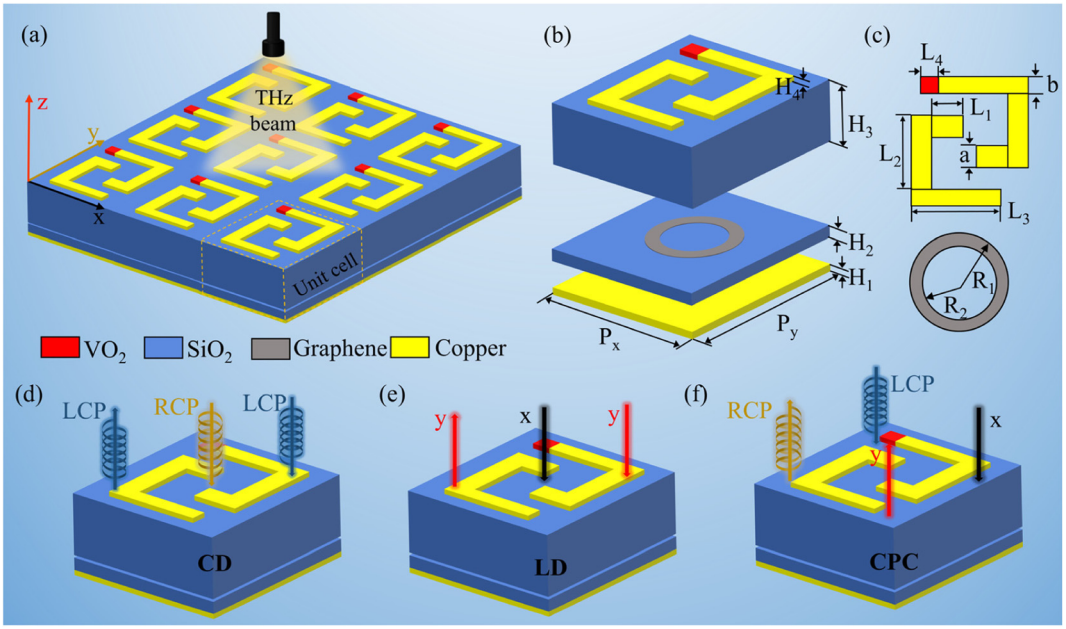

Fig. 1 Metasurface proposed: (a)–(c) are schematic diagrams of the periodic array, unit cell, and the structure of the top resonant layer and graphene ring layer; (d)–(f) are schematic diagrams of CD, LD, and polarization conversion functions.

Table 1 Summary of optimized structural parameters for the proposed metasurface

Parameters	P_x	P_y	H_1	H_2	H_3	H_4	a
Value/μm	56	49	2	3	11.5	2	6
	b	L_1	L_2	L_3	L_4	R_1	R_2
	5	9	22	29	5	9	8

Based on the completed structural design, the fabrication process of the proposed structure was illustrated in combination with mature nano-fabrication technologies, as shown in Fig. 2. First, the silicon substrate is subjected to a cleaning process and subsequently dried. Then, copper film is deposited onto the silicon substrate as the bottom reflective layer using electron beam evaporation (a physical vapour deposition technique, PVD).[37] Next, the first SiO_2 dielectric layer is deposited on the copper layer using plasma-enhanced chemical vapor deposition (PECVD).[38] After that, a single layer of graphene is prepared *via* chemical vapor deposition (CVD)[39] and transferred onto the surface of the SiO_2 layer, and then patterned using electron beam lithography (EBL)[40] and oxygen plasma etching (OPE)[41] techniques. Following this, the second SiO_2 dielectric layer is formed atop the graphene layer *via* PECVD. Finally, the top resonant layer is fabricated: first, the double J-shaped copper elements are fabricated using photolithography, PVD, and lift-off processes, and then the VO_2 structure is formed in designated areas through pulsed laser deposition (PLD)[42] and reactive ion etching (RIE).[43]

In the simulation experiments, copper was assigned a conductivity of 5.8×10^7 S m^{-1}, and SiO_2 was given a permittivity of 3.9. The electrical properties of VO_2 in the THz range are characterized by the Drude model.[44] Its complex dielectric constant can be expressed as:

$$\varepsilon(\omega) = \varepsilon_\infty - \frac{{\omega_p}^2(\sigma)}{(\omega^2 + i\gamma\omega)} \quad (1)$$

$${\omega_p}^2(\sigma) = \frac{\sigma_{VO_2}}{\sigma_0}{\omega_p}^2(\sigma_0) \quad (2)$$

where $\varepsilon_\infty = 12$ is the dielectric constant at high frequency, $\gamma = 5.75 \times 10^{13}$ rad s^{-1} is the collision frequency, $\sigma_0 = 3 \times 10^5$ S m^{-1} is the reference conductivity, and $\omega_p(\sigma_0) = 1.4 \times 10^{15}$ rad s^{-1} denotes the plasma frequency for the reference conductivity. $\omega_p(\sigma)$ is the plasma frequency, and its value is related to the conductivity of VO_2. In this study, we primarily focus on the control effect of VO_2 on the metasurface before and after the phase transition. At 300 K, VO_2 is in its insulating phase; when the temperature exceeds 340 K, it transitions to the metallic phase. The conductivity values for VO_2 in these two phases are 200 S m^{-1} and 200 000 S m^{-1}, respectively.

Within the THz frequency range, the physical properties of graphene are described through its conductivity and dielectric constant.[45,46] Since the intra-band conductivity σ_{intra} of graphene is much greater than the inter-band conductivity σ_{inter} in this frequency range, the influence of σ_{inter} can be ignored. The total conductivity σ_{gra} of graphene can be calculated using the Kubo formula:[47]

$$\begin{aligned}\sigma_{gra} &= \sigma_{intra} + \sigma_{inter} \approx \sigma_{intra} \\ &= -j\frac{e^2 K_B T}{\pi\hbar^2(\omega - j\tau^{-1})} \\ &\quad \times \left[\frac{u_c}{K_B T} + 2\ln\left[\exp\left(-\frac{u_c}{K_B T}\right) + 1\right]\right]\end{aligned} \quad (3)$$

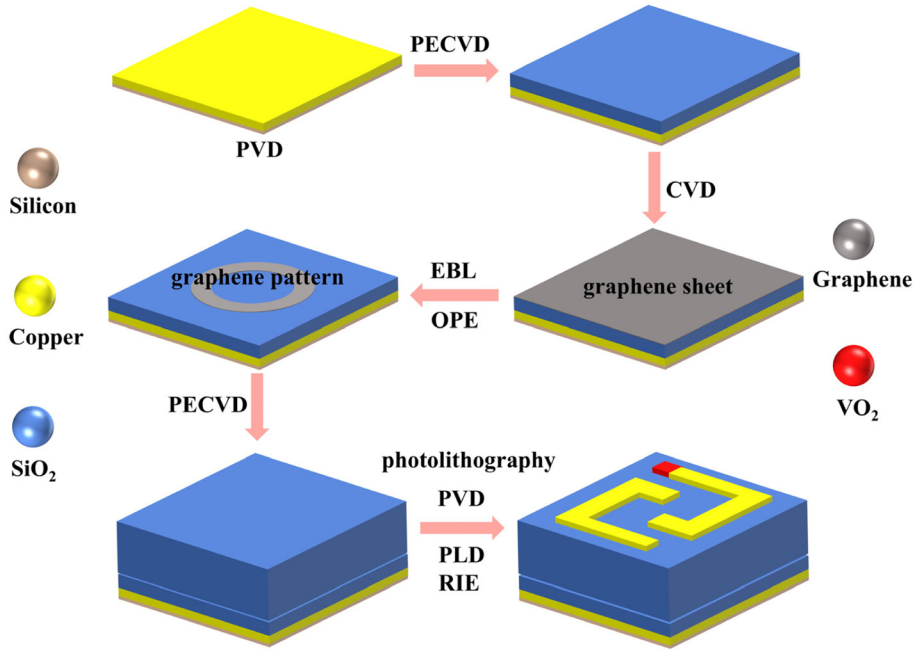

Fig. 2 Schematic illustration of the preparation process of the proposed metasurface.

where e is the electron charge, T is the temperature in Kelvin, K_B is the Boltzmann constant, $\hbar$ is the reduced Planck constant, u_c is the chemical potential of graphene (*i.e.*, the Fermi level E_f), and τ is the relaxation time of the electrons. In the simulation experiments, the relaxation time τ = 1 ps. The dielectric constant of graphene is calculated using the following formula:

$$\varepsilon_{gra} = \varepsilon_0 - j\frac{\sigma_{gra}}{\omega t} \quad (4)$$

where ε_0 is the dielectric constant of free space, and t is the thickness of the graphene layer. In practical implementations, the tuning of the graphene Fermi level can be achieved through electrostatic gating, such as applying a bias voltage between the graphene layer and an underlying gate electrode, which allows continuous modulation of its surface conductivity.[48,49] Meanwhile, the phase transition of VO_2 can be effectively controlled by external thermal stimuli, electrical Joule heating, enabling reversible switching between its insulating and metallic states.[50,51]These mature and well established control methods facilitate the practical implementation of the proposed metasurface in terahertz applications.

In this study, we use CST software to model and simulate the designed metasurface. The basic unit of the model is the periodic structure unit, with the following boundary conditions: periodic boundary conditions are applied along the x and y directions to simulate an infinite planar array structure, and an open boundary is set along the z direction to allow for the natural incidence and transmission of electromagnetic waves. A normally incident plane wave propagating along the $-z$ direction is used in the simulations.

3. Results and discussion

3.1 Dichroism

To facilitate understanding of the working mechanism of the proposed multifunctional metasurface in realizing triple-band CD functionality and single-band LD functionality, we first introduce and analyze the basic concept of dichroism and its mathematical description. Dichroism mainly reflects the difference in the structure's absorption of electromagnetic waves with distinct polarization states, and is typically divided into circular dichroism and linear dichroism. LD represents the difference between the absorption of x-polarized and y-polarized light by the device, and is usually represented as:

$$LD = A_x - A_y \quad (5)$$

where A_x and A_y represent the absorption rates of x-polarized and y-polarized light, respectively. Similarly, CD describes the absorption difference between LCP and RCP light by the structure, and is typically defined as:

$$CD = A_{RCP} - A_{LCP} \quad (6)$$

In the equation, A_{LCP} and A_{RCP} represent the absorption rates of LCP and RCP light, respectively.

Under the condition of circularly polarized (CP) light incidence, the incident and reflected fields are described using the Jones matrix.[52] The reflection process satisfies:

$$\begin{pmatrix} E_r^{LCP} \\ E_r^{RCP} \end{pmatrix} = \begin{pmatrix} r_{LL} & r_{LR} \\ r_{RL} & r_{RR} \end{pmatrix} \begin{pmatrix} E_i^{LCP} \\ E_i^{RCP} \end{pmatrix} = R_{circ} \begin{pmatrix} E_i^{LCP} \\ E_i^{RCP} \end{pmatrix} \quad (7)$$

where E_i and E_r represent the electric field vectors of the incident and reflected light, respectively, and R_{circ} is the reflection

matrix under the circular polarization basis. When the incident light is linearly polarized (LP), the corresponding reflection matrix R_{lin} can be expressed as:

$$R_{\text{lin}} = \begin{pmatrix} r_{xx} & r_{xy} \\ r_{yx} & r_{yy} \end{pmatrix} \tag{8}$$

To better understand the correspondence between the linear polarization basis and the circular polarization basis, the linear basis is transformed into the circular one through a basis conversion. Using the normalization transformation matrix $\Lambda = \frac{1}{\sqrt{2}} \begin{pmatrix} 1 & 1 \\ -i & i \end{pmatrix}$, R_{circ} can be expressed as:

$$\begin{aligned} R_{\text{circ}} &= \begin{pmatrix} r_{\text{LL}} & r_{\text{LR}} \\ r_{\text{RL}} & r_{\text{RR}} \end{pmatrix} = \Lambda^{-1} R_{\text{lin}} \Lambda \\ &= \frac{1}{2} \begin{pmatrix} r_{xx} - r_{yy} - i(r_{xy} + r_{yx}) & r_{xx} + r_{yy} + i(r_{xy} - r_{yx}) \\ r_{xx} + r_{yy} - i(r_{xy} - r_{yx}) & r_{xx} - r_{yy} + i(r_{xy} + r_{yx}) \end{pmatrix} \end{aligned} \tag{9}$$

Here, $r_{\text{LL}}(r_{xx})$ and $r_{\text{RR}}(r_{yy})$ denote the reflection coefficients for the co-polarized components, while $r_{\text{LR}}(r_{xy})$ and $r_{\text{RL}}(r_{yx})$ correspond to the cross-polarized components. Because the copper substrate is far thicker than the penetration depth of the THz wave, the transmission rate is effectively negligible ($T \approx 0$). Therefore, its absorption rate A can be obtained from the reflection rate R:

$$A = 1 - R \tag{10}$$

In the equation, $R = |r|^2$. Thus, the absorption rate can be expressed as:

$$A_x = 1 - R_{xx} - R_{yx} = 1 - |r_{xx}|^2 - |r_{yx}|^2 \tag{11}$$

$$A_y = 1 - R_{yy} - R_{xy} = 1 - |r_{yy}|^2 - |r_{xy}|^2 \tag{12}$$

$$A_{\text{LCP}} = 1 - R_{\text{LL}} - R_{\text{RL}} = 1 - |r_{\text{LL}}|^2 - |r_{\text{RL}}|^2 \tag{13}$$

$$A_{\text{RCP}} = 1 - R_{\text{RR}} - R_{\text{LR}} = 1 - |r_{\text{RR}}|^2 - |r_{\text{LR}}|^2 \tag{14}$$

3.1.1 Switchable triple-band CD response. To analyze the CD response characteristics of the proposed metasurface under normal incidence of CP light, Fig. 3 shows the reflectance, absorbance, and CD response curves of VO_2 in different phases. For clarity, the analysis is divided into two parts: first, the triple-band CD mode (Mode 1) corresponding to the metallic phase is discussed, followed by the single-band CD mode (Mode 2) under the insulating phase.

Under the VO_2 metallic phase together with a graphene Fermi level (E_f) of 0.8 eV, the corresponding reflectance, absorbance, and CD response curves of the metasurface are shown in Fig. 3(a)–(c). From Fig. 3(a), it can be seen that the co-polarized reflectance is equal over the entire operating frequency range. However, there is a significant difference between the cross-polarized reflectances. In particular, at f_1 = 1.62 THz, f_2 = 2.89 THz, and f_3 = 3.19 THz, the difference between the cross-polarized reflectances R_{LR} and R_{RL} is most pronounced, leading to a strong triple-band narrowband CD response. As shown in Fig. 3(b), at frequencies f_1, f_2, and f_3, the structure exhibits a pronounced difference in the absorption of RCP and LCP light. Specifically, at f_1, f_2, and f_3, the absorption rates of RCP light reach 98.9%, 91.1%, and 95.9%, respectively, far exceeding the LCP absorption levels of 4.5%, 8.1%, and 7.9%. This absorption difference directly leads to a strong CD effect. As shown in Fig. 3(c), the structure exhibits distinct narrowband CD peaks at f_1, f_2, and f_3 (denoted as I, II, and III), with peak values of 0.944, 0.83, and 0.88, respectively, indicating that the structure demonstrates a significant triple-band CD response in the VO_2 metallic phase.

Under the VO_2 insulating phase and E_f = 1.0 eV, the CD response characteristics of the device undergo significant changes. The corresponding reflectance, absorbance, and CD response curves are presented in Fig. 3(d–f). As depicted in Fig. 3(d), compared to the metallic phase, the co-polarized reflectance remains almost unchanged, while the cross-polarized reflectance is enhanced at all three resonance frequencies, especially at the last two frequencies. Meanwhile, the positions of the resonance peaks shift slightly, with the new frequencies being f_4 = 1.6 THz, f_5 = 2.83 THz, and f_6 = 3.08 THz. Furthermore, as depicted in Fig. 3(e) and (f), the absorption intensity of LCP light changes little, while the absorption intensity of RCP light significantly decreases, maintaining a higher absorption level only around f_4. This leads to the weakening of the original triple-band CD mode, with a high CD value of 0.91 at f_4, while the CD values at the other two frequencies fall below 0.41. This variation primarily results from the transition of VO_2 from the metallic phase to the insulating phase, which alters the resonance conditions of the structure. Since a high CD response is maintained only at f_4, and the CD responses at f_5 and f_6 are weaker, the structure can be considered a single-band CD mode when VO_2 is in the insulating phase.

Under the VO_2 metallic phase, to further investigate the role of graphene in modulating the device's CD response, the effect of the variation in its Fermi level on the CD response was studied. As shown in Fig. 4, with the gradual decrease of E_f, both the frequency positions and CD intensities of the three resonance peaks change. Specifically, the change in peak I is relatively small, with the CD intensity slightly decreasing but still remaining above 0.9, and only a slight redshift in frequency. In contrast, the changes in peaks II and III are more significant: as E_f decreases, the CD intensity of peak II gradually weakens and eventually disappears, accompanied by a noticeable redshift. For peak III, as E_f decreases from 0.8 eV down to 0.2 eV, its CD intensity shows a progressive reduction; when E_f further drops to 0.1 eV, the CD intensity begins to recover. Meanwhile, the resonance frequency continues to redshift as E_f decreases. As shown, tuning the graphene Fermi level enables different degrees of control over the three CD peaks. It is worth noting that when E_f = 0.1 eV, the device exhibits a dual-band CD mode (Mode 3), with corresponding CD intensities of 0.913 and 0.754. In summary, through the joint modulation of VO_2 and graphene, the device's CD response can be actively switched between Mode 1, Mode 2, and Mode 3. This method overcomes the limitations of traditional metasurfaces, where the number of CD peaks is fixed and non-

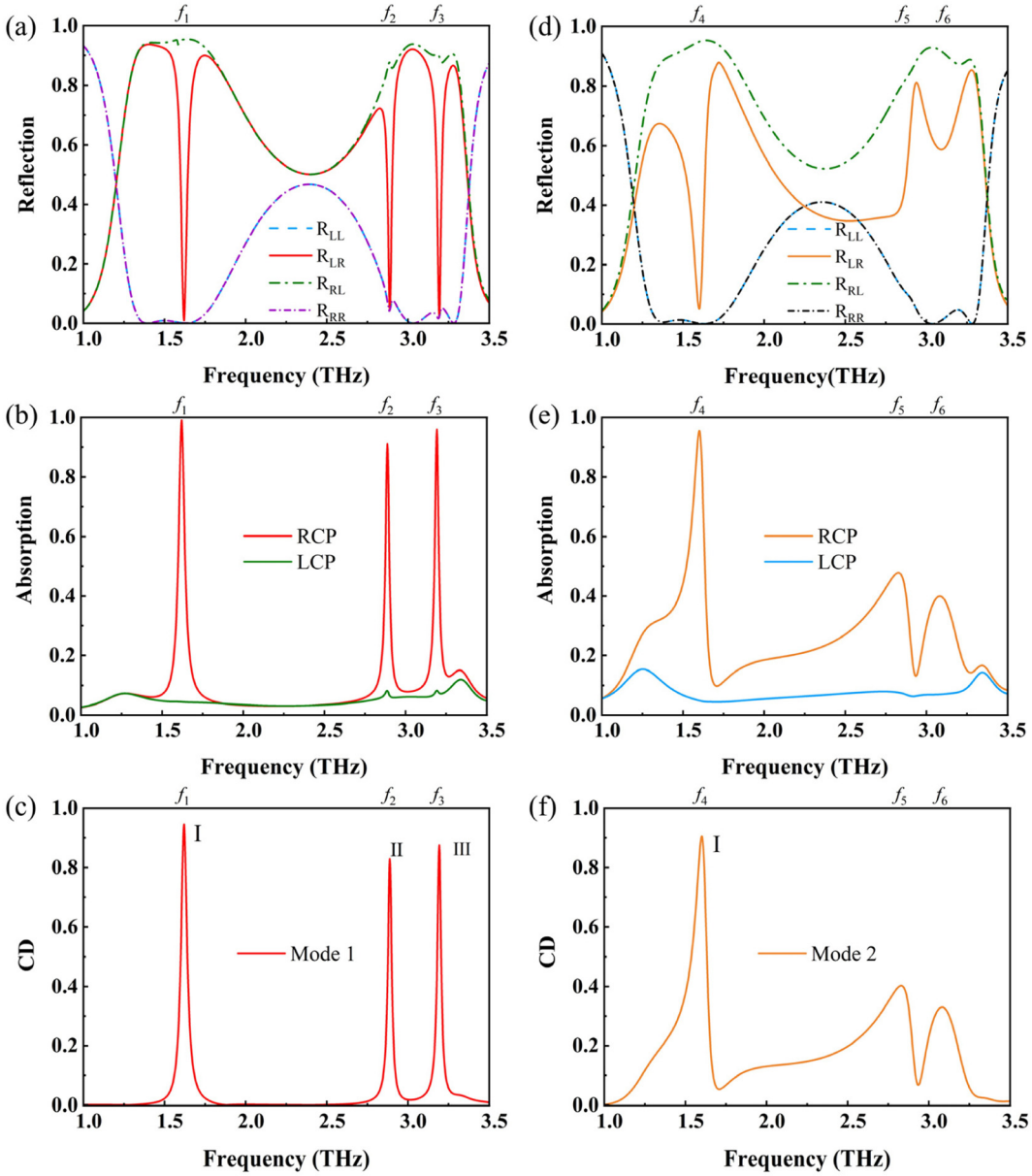

Fig. 3 Reflectance, absorbance, and CD response curves of the metasurface: (a)–(c) results for the VO_2 metallic phase; (d)–(f) results for the VO_2 insulating phase.

tunable, offering a new idea for the control of CD response in terahertz chiral metasurfaces.

To further reveal the physical mechanism behind the strong circular dichroism of the device, Mode 1 is selected as a representative for electric field distribution analysis. It should be noted that both Mode 2 and Mode 3 are evolved from Mode 1 under different modulation conditions. Therefore, as a triple-resonance mode in the complete state, Mode 1 can comprehensively reflect the formation mechanism of the device's circular dichroism and is representative for understanding the entire tunable process.

Fig. 5 presents the electric-field patterns corresponding to the three resonance frequencies f_1, f_2, and f_3 under normal LCP and RCP light incidence in Mode 1, including the planar distribution of the top resonant layer and the side view along the xz direction. As shown in Fig. 5(a–c), under LCP light incidence, the overall electric field intensity at the three resonance frequencies is relatively weak, mainly concentrated at the edge regions of the top metallic resonant units. At this time, the impedance matching between the incident light and the structure is poor, resulting in strong reflection and weak absorption. In contrast, under RCP light incidence, the electric field intensity is significantly enhanced with a wider distribution range, exhibiting a typical strong coupling characteristic, as displayed in Fig. 5(d–f). At f_1, the electric field is mainly distributed at the edges of the upper and lower J-shaped copper

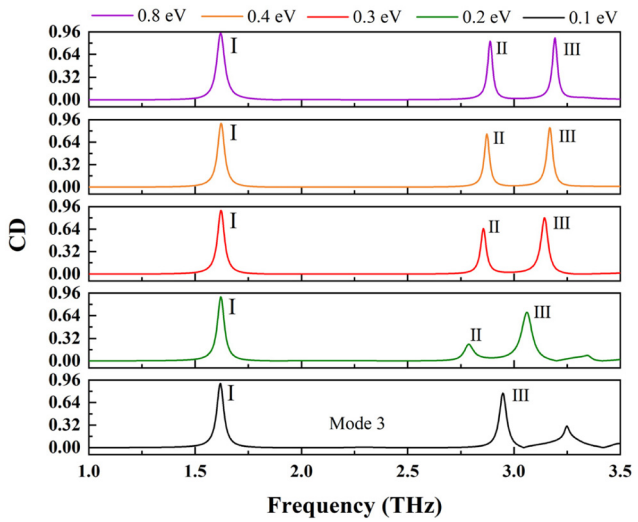

Fig. 4 Effect of varying the graphene Fermi level on the metasurface CD response under the VO_2 metallic phase.

elements and the VO_2 patches, indicating that the energy is primarily absorbed through the electric dipole mode of the top resonant unit. At f_2, the electric field is primarily concentrated at the edges of the upper and lower J-shaped copper elements, around the VO_2 patches, and within the dielectric layer above the graphene ring. Among these regions, the electric field intensity inside the dielectric layer is the most pronounced. From the side view of the *xz* cross-section, a clear standing-wave node–antinode pattern can be observed inside the dielectric layer. This indicates that the resonance at this frequency results from the coupling between the top electric dipole resonance and the Fabry–Pérot (FP) cavity resonance,[53] forming a hybrid mode dominated by the FP cavity effect. At f_3, the electric field is primarily concentrated in the dielectric layer regions above and below the graphene ring, as well as in the upper J-shaped copper element and VO_2 patches. Among them, the top resonant layer exhibits the strongest electric field intensity. This suggests that the resonance at this frequency is also a hybrid mode formed by the coupling between the top electric dipole resonance and the FP cavity resonance, but dominated by the top electric dipole resonance.

In summary, the resonance under LCP light incidence is relatively weak, while RCP light incidence produces stronger localized fields and cavity resonances. The significant difference between the two leads to pronounced circular dichroism at all three frequencies. Furthermore, by regulating the VO_2 phase state and the graphene Fermi level, the equivalent impedance of the resonant unit can be effectively tuned, thereby altering the electromagnetic coupling state between the resonant unit and

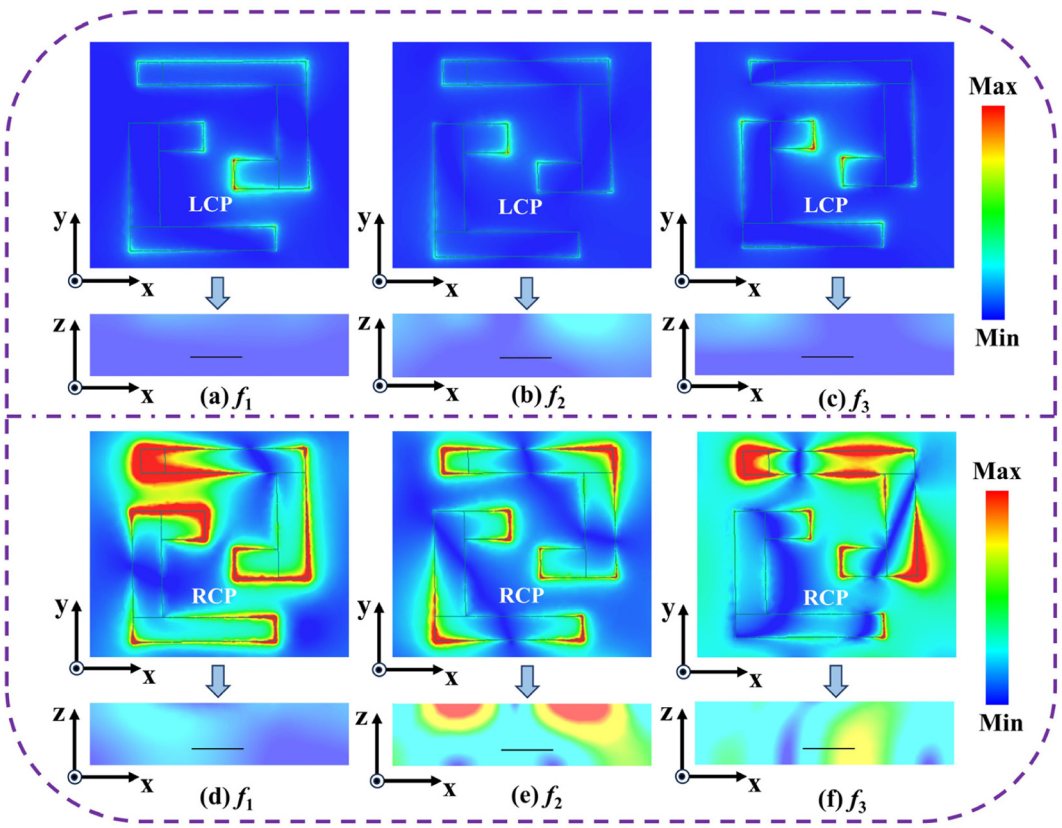

Fig. 5 Electric field patterns of the resonant layer and the *xoz*-plane under Mode 1: (a–c) field distribution under LCP light incidence; (d–f) field distribution under RCP light incidence.

the cavity. As a result, controllable switching between triple-band, dual-band, and single-band CD modes can be achieved.

To assess the metasurface's robustness against variations in the incident azimuth, we further analyzed the CD responses at different azimuth angles, as shown in Fig. 6. Overall, the resonance peak positions in the three operating modes are almost unchanged with φ, showing only slight fluctuations in intensity, which indicates that the CD response of this structure is stable under different incident azimuths. Therefore, we consider that this metasurface can maintain a stable narrowband strong CD effect over a wide azimuth range and has good application potential in direction-sensitive devices such as multi-frequency detectors.

3.1.2. Reversible single-band LD response. Under the VO_2 insulating phase and E_f = 1.0 eV, the designed metasurface exhibits a distinct single-band LD effect. As shown in Fig. 7(a), the device demonstrates significant absorption for x-polarized light at f = 4.093 THz, while almost total reflection occurs for y-polarized light. Specifically, R_{xx} drops below 0.1 at this frequency, whereas R_{yy} remains above 0.98, and the cross-polarized reflection coefficients R_{xy} and R_{yx} are both close to zero. To more intuitively analyze the absorption characteristics of the device, the absorption and LD curves were calculated, as displayed in Fig. 7(b). Fig. 7(b) shows that for f = 4.093 THz, the absorption of x-polarized light (A_x) reaches a peak value of 0.92, while that of y-polarized light (A_y) is only 0.02, corresponding to an LD value as high as 0.90. This indicates that the device can efficiently distinguish between different linearly polarized terahertz waves, showing potential application value in polarization control and related optoelectronic devices. Furthermore, Fig. 7(c and d) illustrates that the LD intensity of the proposed metasurface is dynamically tunable through adjusting the Fermi level of graphene. As illustrated in Fig. 7(c), the LD gradually decreases with the reduction of E_f, and when E_f = 0.2 eV, the amplitude of LD approaches zero. Fig. 7(d) shows that as E_f decreases, the LD intensity weakens progressively, accompanied by an obvious redshift in the resonance frequency. The highest and lowest LD values reach 0.9 and 0.076, enabling the LD function to switch between its "on" and "off" states. This provides a new idea for designing terahertz switching devices.

To reveal the underlying mechanism responsible for the strong LD effect, the impedance characteristics of the device are first analyzed. According to the impedance matching theory, when the effective impedance (Z) of the metasurface matches the free-space impedance (Z_0), that is, when the real part of the relative impedance (Z_r) approaches 1 and the imaginary part approaches 0, the reflection can be effectively suppressed, thereby achieving high absorption. According to effective medium theory,[54] the relative impedance Z_r of the

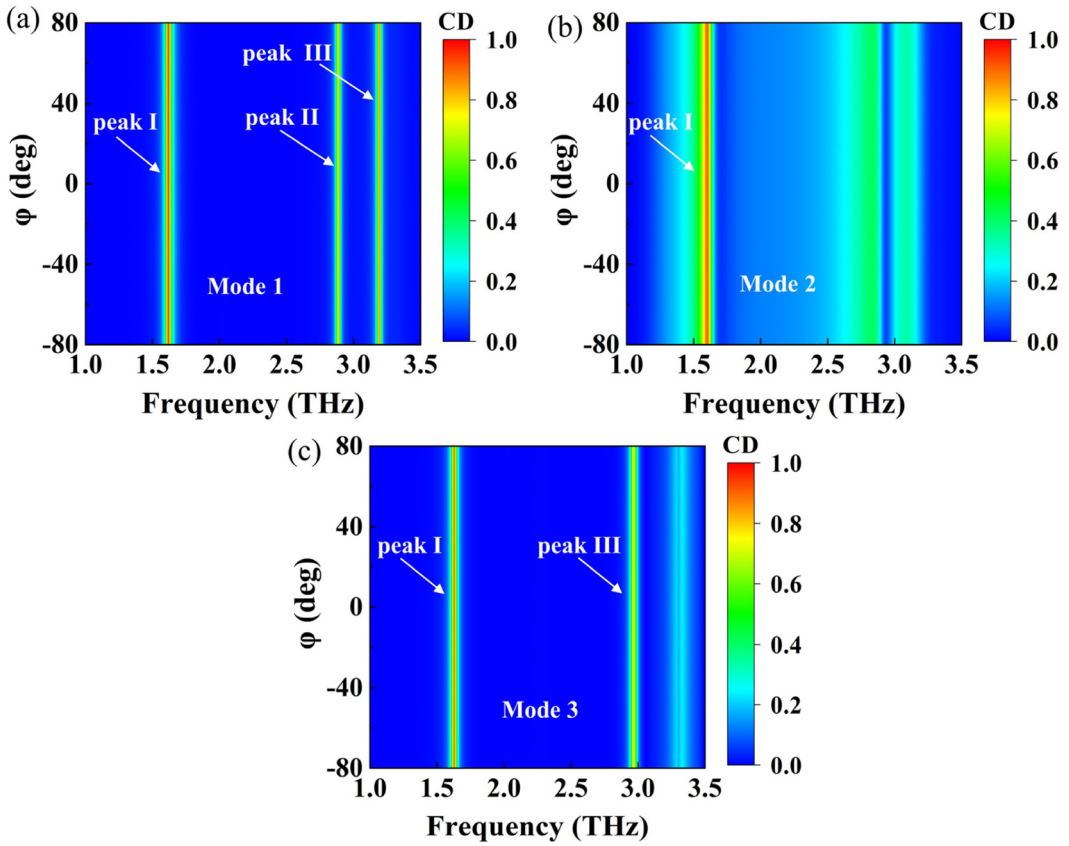

Fig. 6 CD responses under different azimuth angles for three modes: (a) Mode 1, (b) Mode 2, and (c) Mode 3.

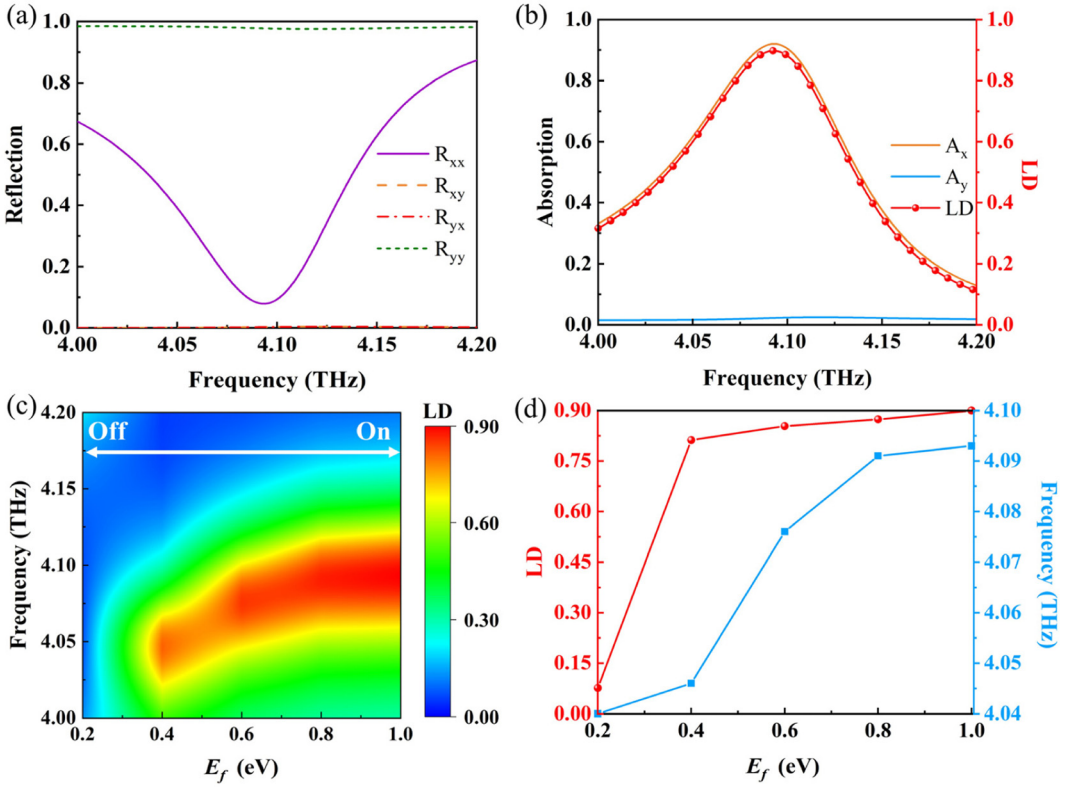

Fig. 7 Electromagnetic response characteristics of the metasurface under LP light: (a) reflectivity; (b) absorptivity and LD response; (c) LD response at different Fermi levels; (d) influence of Fermi level on LD response and resonance frequency.

metasurface can be retrieved from the *S*-parameters, and its expression is given as:

$$Z_r = \frac{Z}{Z_0} = \sqrt{\frac{(1+S_{11})^2 - (S_{21})^2}{(1-S_{11})^2 - (S_{21})^2}} \quad (15)$$

Here, S_{11} and S_{21} represent the reflection and transmission coefficients, respectively. Since a copper reflective layer is employed at the bottom of the structure, the transmission coefficient is nearly zero, and thus the relative impedance is mainly determined by the reflection characteristics.

As shown in Fig. 8, the relative impedance curves of the metasurface under normal incidence of *x*-polarized and *y*-polarized light are presented. From Fig. 8(a), it can be observed that when *x*-polarized light is incident, the real part of the relative impedance approaches 1 and the imaginary part

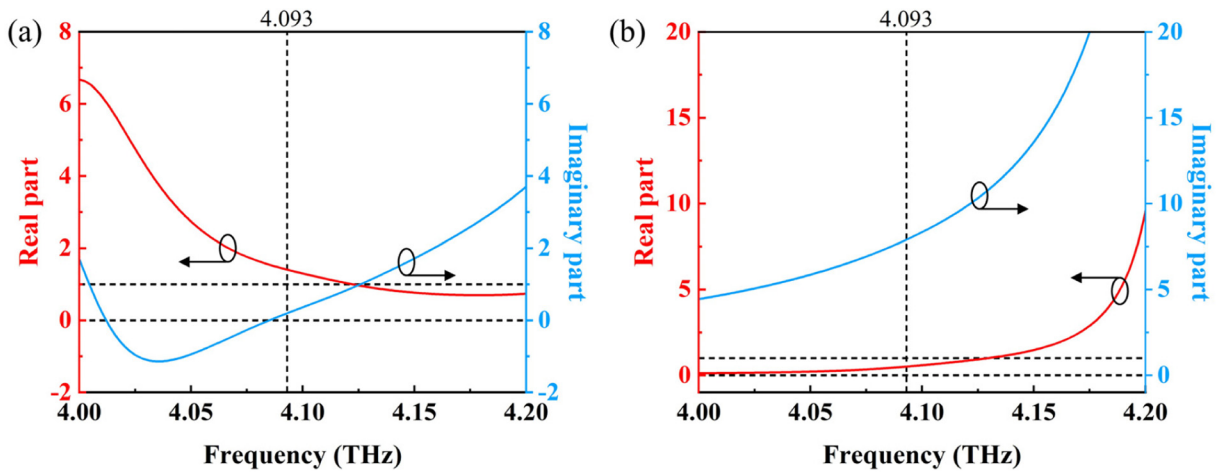

Fig. 8 Relative impedance of the metasurface under different polarization incidences: (a) *x*-polarized light; (b) *y*-polarized light.

approaches 0 at f = 4.093 THz, indicating that the effective impedance of the device is well matched with the free-space impedance, thereby effectively suppressing reflection and achieving nearly perfect absorption. In contrast, when y-polarized light is incident, Fig. 8(b) indicates that although the real part of the impedance is likewise close to 1 at f = 4.093 THz, its imaginary part deviates significantly from 0, indicating that the impedance matching condition is not satisfied. Therefore, compared with x-polarized light, the energy coupling efficiency of y-polarized light is considerably reduced, and the absorption effect is notably weakened, resulting in a pronounced LD effect at this frequency.

To further elucidate the underlying physical mechanism underlying the LD response, Fig. 9 presents the electric field distributions of the metasurface at f = 4.093 THz under normal incidence with x- and y-polarized light, including the planar distribution of the top resonant layer and the side view along the xz direction. As depicted in Fig. 9(a), under x-polarized light incidence, the electric field is mainly distributed at the edges of the upper J-shaped copper element, the VO_2 patches, and the dielectric region above the graphene ring. This indicates that the incident energy is effectively coupled into the structure, forming a hybrid mode generated by the coupling between the top electric dipole resonance and the FP cavity, which leads to strong absorption characteristics. In contrast, as shown in Fig. 9(b), when y-polarized light is incident, the overall electric field intensity is relatively weak and mainly distributed along the horizontal edges of the two J-shaped copper elements, with almost no significant field distribution observed inside the dielectric layer. This indicates that the impedance matching between the incident light and the structure is poor at this time, resulting in limited coupling and most of the energy being reflected. It is precisely this significant difference in absorption capability for different linearly polarized light that gives rise to the pronounced LD effect at this frequency.

Next, the LD responses of the incident linearly polarized light under various polarization angles were evaluated, as illustrated in Fig. 10. As illustrated in Fig. 10(a), when φ = 0°, the metasurface exhibits an LD value of 0.90 at f = 4.093 THz, whereas when φ = −80°, the LD value at the same frequency reaches −0.89. It can be seen that with the variation of the polarization angle, the metasurface exhibits a reversible change in its LD value from 0.90 to −0.89 at the same frequency. In addition, Fig. 10(b) illustrates that variations in the polarization angle φ cause the LD value to undergo a reversible transition from negative to positive and then back to negative within the same frequency range. This demonstrates that the designed metasurface supports a single-band reversible LD switching function, indicating its potential application value in terahertz optical switches and polarization control devices.

3.2 Polarization conversion

When VO_2 is in the insulating phase and E_f = 1.0 eV, the designed metasurface can also realize linear-to-linear and circular-to-circular polarization conversion functions. To better evaluate the polarization conversion performance of the device, the concept of polarization conversion rate (PCR) is introduced. PCR is defined as the ratio of the cross-polarized reflectivity to the total reflectivity, which can be expressed as:[55]

$$\mathrm{PCR} = \frac{|r_{\mathrm{cross}}|^2}{|r_{\mathrm{cross}}|^2 + |r_{\mathrm{co}}|^2} \tag{16}$$

Here, r_{cross} and r_{co} represent the cross-polarized and co-polarized reflection coefficients, respectively. When the PCR approaches 1, this implies that the incident light is almost completely converted into its orthogonal polarization state.

As demonstrated in Fig. 11(a and b), when x-polarized light is incident, the device achieves efficient polarization conversion in two frequency bands of 1.26–1.59 THz and 2.9–3.31 THz, with the PCR remaining above 0.8 throughout both bands. This is because at this time, the co-polarized reflectivity R_{xx} approaches 0, and the total reflectivity is almost entirely determined by the cross-polarized reflectivity R_{yx}, thereby maintaining a high PCR level. This indicates that the incident x-polarized light is effectively converted into y-polarized light within these two frequency bands. Furthermore, as demon-

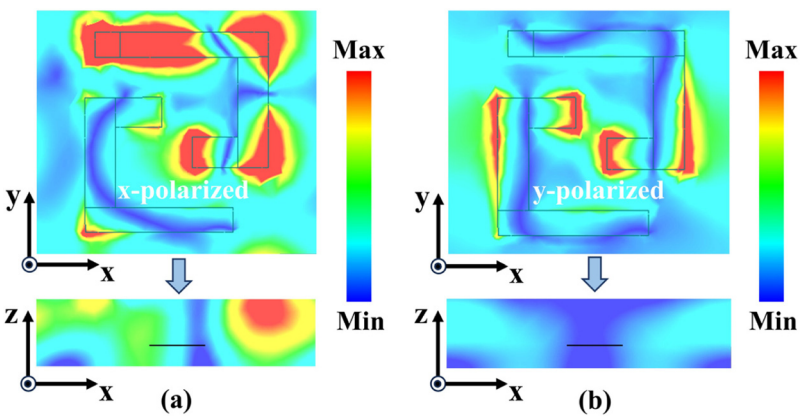

Fig. 9 Electric field distributions of the metasurface under different LP light incidences: (a) x-polarized light; (b) y-polarized light.

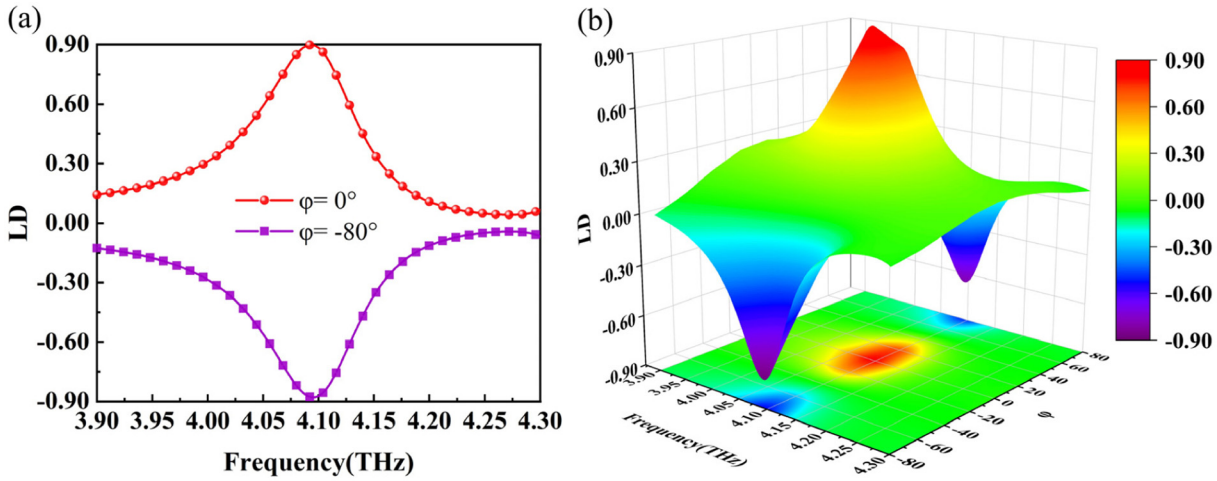

Fig. 10 LD response characteristics of the metasurface under various polarization angles: (a) reversible two-dimensional LD curve; (b) three-dimensional LD distribution.

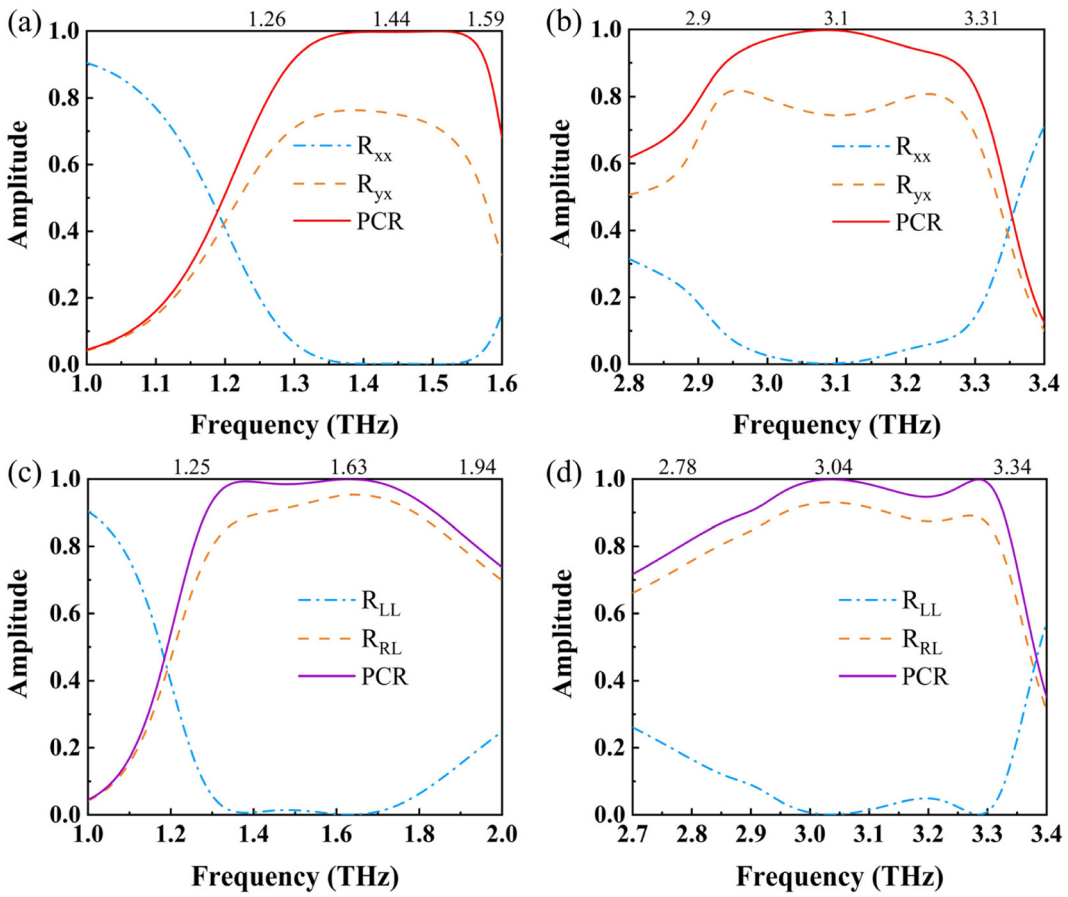

Fig. 11 Co-polarized reflectivity, cross-polarized reflectivity, and PCR values of the metasurface under different polarized light incidences: (a and b) *x*-polarized light; (c and d) LCP light.

strated in Fig. 11(c–d), when LCP light is incident, the device achieves efficient polarization conversion in two frequency bands of 1.25–1.94 THz and 2.78–3.34 THz, with the PCR remaining above 0.8 throughout both bands. Similarly, this is because at this time, the co-polarized reflectivity R_{LL} approaches 0, and the total reflectivity is almost entirely determined by the cross-polarized reflectivity R_{RL}, thereby maintaining a high PCR level. It can thus be seen that the incident LCP

light is effectively converted into RCP light within these two frequency bands.

To further elucidate the mechanism responsible for the linear-to-linear polarization conversion, Fig. 12 displays the surface current patterns of the structure at the peak frequencies of the two operating bands. The black arrows indicate the flow direction of the equivalent surface current. As observed from Fig. 12(a–c), at f_7 = 1.44 THz, the equivalent current direction of the top resonant layer is opposite to that of the equivalent currents on the graphene ring and the bottom copper substrate, while the equivalent current directions of the graphene ring and the bottom copper substrate are consistent. The antiparallel currents excite magnetic dipole resonance, whereas the parallel currents excite electric dipole resonance. Consequently, the efficient polarization conversion at f_7 is caused by the combined effect of electric dipole resonance and magnetic dipole resonance. As observed from Fig. 12(d–f), at f_8 = 3.1 THz, the equivalent current direction of the top resonant layer is consistent with that of the equivalent currents on the graphene ring and the bottom copper substrate. Since the current directions of all layers are the same, an electric dipole resonance is excited. As a result, the efficient polarization conversion at f_8 is caused by the electric dipole resonance.

Similarly, the mechanism responsible for circular-to-circular polarization conversion can also be explained by the surface current distribution. Fig. 13 shows the surface current distributions of each layer at the peak frequencies under normal incidence of LCP light. As observed from Fig. 13(a–c), at f_9 = 1.63 THz, the equivalent current on the upper resonant layer flows in the opposite direction to the equivalent currents on the graphene ring and the bottom copper substrate, while the current directions on the graphene ring and the bottom copper substrate remain consistent. The antiparallel currents excite magnetic dipole resonance, whereas the parallel currents excite electric dipole resonance. Therefore, similar to f_7, the efficient polarization conversion at f_9 is also caused by the combined effect of electric dipole resonance and magnetic dipole resonance. As observed from Fig. 13(d–f), at f_{10} = 3.04 THz, the direction of the equivalent current on the upper resonant layer aligns with that of the equivalent currents on the graphene ring and the bottom copper substrate. Since the current directions of all layers are the same, an electric dipole resonance is excited. Therefore, similar to f_8, the efficient polarization conversion at f_{10} is also caused by the electric dipole resonance.

Finally, to more intuitively demonstrate the advantages of the proposed multifunctional metasurface, a comparative analysis with previously reported related works was conducted (see Table 2). As shown in Table 2, most of the reported terahertz chiral metasurfaces achieve only one or two CD peaks, and the peak intensities are generally below 0.9. In contrast, the proposed metasurface realizes three distinct CD peaks in the terahertz band, with maximum values of 0.944, 0.83, and 0.88, respectively, exhibiting a stronger multi-frequency CD response. This enables the metasurface to achieve efficient chiral responses at multiple operating frequencies, showing greater advantages in applications such as multichannel filtering, chiral molecule detection, and terahertz imaging. Meanwhile, the structure also possesses LD and polarization conversion functions and exhibits good tunability. This endows it with significant advantages in multifunctional integration and performance regulation. It is worth noting that current research on multi-frequency chiral terahertz metasurfaces remains relatively limited, especially studies that

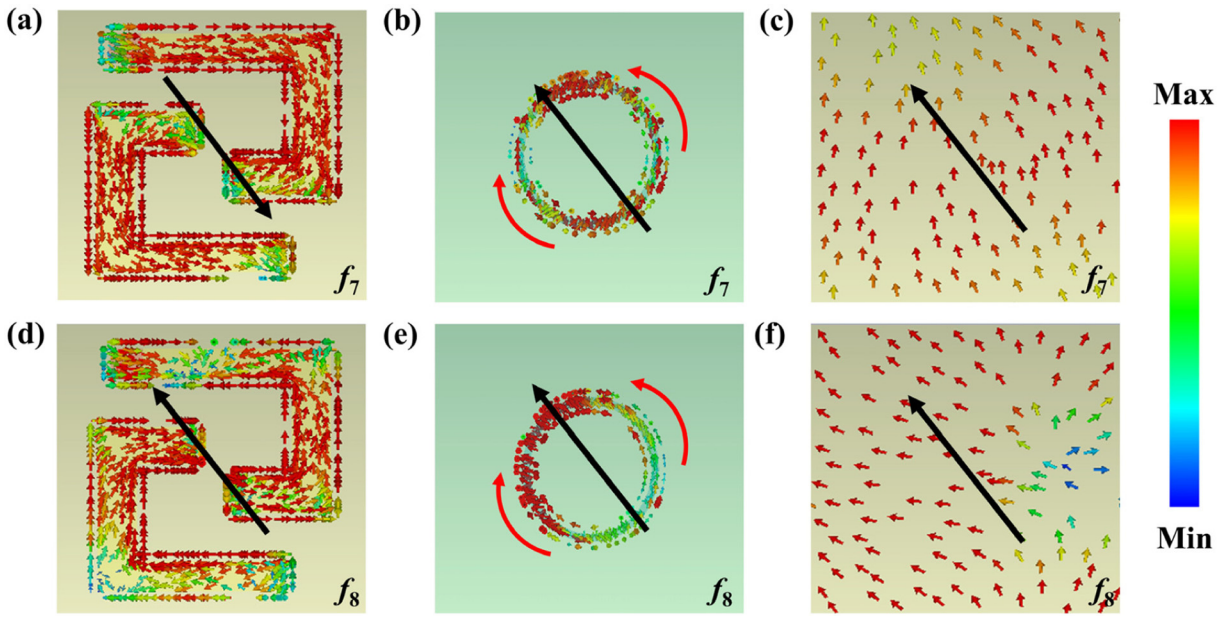

Fig. 12 Surface current distributions of each layer at the peak frequencies under normal incidence of *x*-polarized light: (a–c) f_7 = 1.44 THz; (d–f) f_8 = 3.1 THz.

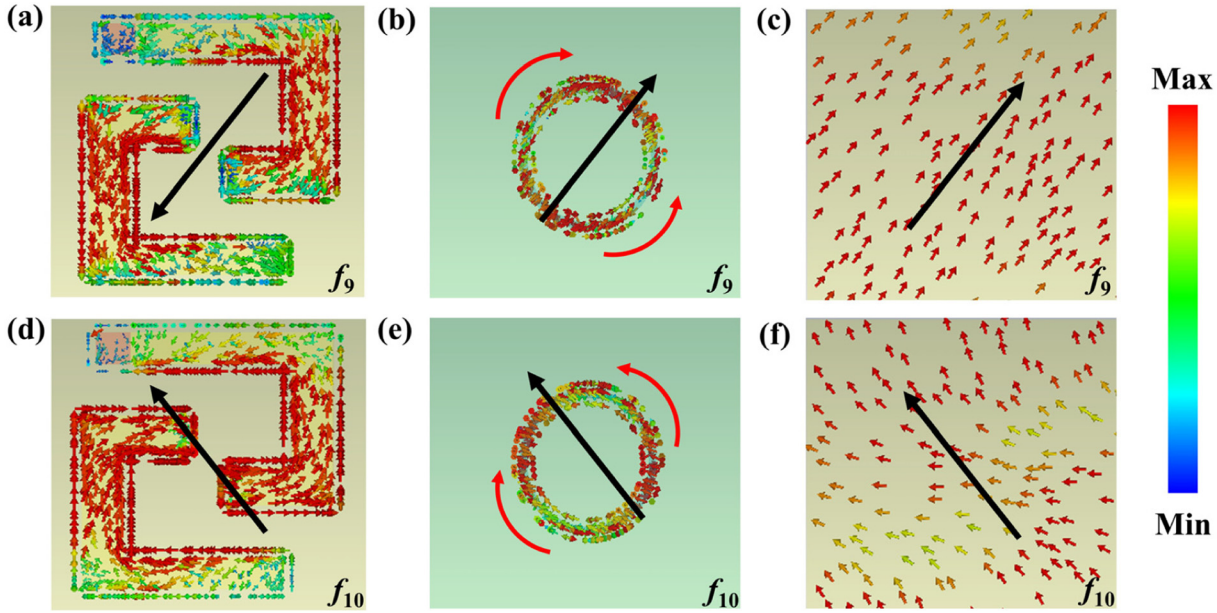

Fig. 13 Surface current distributions of each layer at the peak frequencies under normal incidence of LCP light: (a–c) f_9 = 1.63 THz; (d–f) f_{10} = 3.04 THz.

Table 2 Comparison with previously reported related works

Ref.	CD peaks	CD_{max}	LD peaks	LD_{max}	CPC range (THz)	Tunable
56	3	0.8, 0.66, 0.64	—	—	—	No
57	2	0.89, 0.75	—	—	—	Yes
58	3	0.91, 0.35, 0.87	—	—	—	Yes
59	1	0.89	1	0.87	*x*-to-*y*: 2.80 & 6.87	Yes
60	1	0.75	1	0.74	*x*-to-*y*: 4.1–7.1	Yes
This work	**3**	**0.944, 0.83, 0.88**	**1**	**0.90**	***x*-to-*y*: 1.26–1.59, 2.90–3.31, L-to-R: 1.25–1.94, 2.78–3.34**	**Yes**

combine multi-frequency CD responses with multifunctional integration are even rarer. Therefore, this work provides an important reference value for the multifunctional integration and application of reconfigurable terahertz photonic devices.

4. Conclusion

To sum up, this study innovatively designs a multifunctional reconfigurable THz chiral metasurface based on VO_2 and graphene. By combining the phase transition characteristics of VO_2 and the electrical tunability of graphene, the structure realizes multiple functions, including switchable triple-band CD response, single-band reversible LD response, and efficient linear-to-linear and circular-to-circular polarization conversion. The research results show that:

(1) Under CP light incidence, the metasurface exhibits a significant triple-band CD response in the frequency range of 1.0–3.5 THz. Three distinct CD peaks are generated at 1.62 THz, 2.89 THz, and 3.19 THz, with peak values of 0.944, 0.83, and 0.88, respectively. In addition, through the combined regulation of VO_2 and graphene, dynamic switching of the number of CD peaks can be achieved, overcoming the limitation of conventional metasurfaces, where the number of CD peaks is fixed and non-tunable.

(2) Under LP light incidence, the metasurface exhibits a significant single-band LD response in the frequency range of 4.0–4.2 THz. A distinct LD peak appears at 4.093 THz, with a peak value of 0.9. Moreover, tuning the Fermi level of graphene together with the polarization angle of the incident light enables intensity modulation and reversible switching of the LD response.

(3) When *x*-polarized light is incident, the metasurface achieves efficient polarization conversion in two frequency bands of 1.26–1.59 THz and 2.90–3.31 THz, with the PCR remaining above 80% throughout both bands. Among them, the PCR reaches 100% at 1.44 THz and 3.1 THz, indicating that the incident *x*-polarized light is completely converted into *y*-polarized light at these frequencies. When LCP light is incident, the metasurface achieves efficient polarization conversion in two frequency bands of 1.25–1.94 THz and 2.78–3.34 THz, with the PCR remaining above 80% throughout both bands. Among them, the PCR reaches 100% at 1.63 THz and 3.04 THz, indicating that the incident LCP light is completely converted into RCP light at these frequencies.

Lastly, we consider that the design method proposed in this study promotes the development of the terahertz field and lays a foundation for further research on multifunctional reconfigurable photonic devices.

Author contributions

Hongrun Xu: data curation, writing – original draft preparation. Zhen Cui: supervision, writing – reviewing and editing.

Conflicts of interest

There are no conflicts to declare.

Data availability

All data supporting this study are available within the article.

Acknowledgements

This work was funded by the National Natural Science Foundation of China (No. 62474140) and the Key R&D Program Projects in Shaanxi Province (No. 2024GX-YBXM-087).

References

1 J. Chen, S.-X. Huang, K. F. Chan, G.-B. Wu and C. H. Chan, *Nat. Commun.*, 2025, **16**, 363.
2 Z.-K. Zhang, T. Zhang, Z.-P. Zhang, M.-Z. Chong, M. Xiao, P. Peng, P. Feng, H. Sun, Z. Zheng, X. Zang, Z. Fang and M.-Y. Xia, *Nat. Commun.*, 2025, **16**, 8133.
3 W. Gao, H. Zhang, M. Liu, S. Cheng and Z. Yi, *Dalton Trans.*, 2025, **54**, 15062–15072.
4 G. Zou, T. Liu, C. Wang, C. Luo, Z. Qin, J. Ji and Z. Yi, *Dalton Trans.*, 2025, **54**, 10898–10906.
5 B. Chen, X. Wang, W. Li, C. Li, Z. Wang, H. Guo, J. Wu, K. Fan, C. Zhang, Y. He, B. Jin, J. Chen and P. Wu, *Sci. Adv.*, 2022, **8**, eadd1296.
6 Y. Jo, H. Park, H. Yoon and I. Kim, *Opto-Electron. Adv.*, 2024, **7**, 240122.
7 A. Ahmadivand, B. Gerislioglu, Z. Ramezani, A. Kaushik, P. Manickam and S. A. Ghoreishi, *Biosens. Bioelectron.*, 2021, **177**, 112971.
8 Q. Shangguan, H. Chen, H. Yang, S. Liang, Y. Zhang, S. Cheng, W. Yang, Z. Yi, Y. Luo and P. Wu, *Diamond Relat. Mater.*, 2022, **125**, 108973.
9 Z. Cui, Q. Lu and X. Wang, *Int. J. Imaging Syst. Technol.*, 2026, **36**, e70297.
10 D. R. Smith and N. Kroll, *Phys. Rev. Lett.*, 2000, **85**, 2933–2936.
11 S. L. Zhai, X. P. Zhao, S. Liu, F. L. Shen, L. L. Li and C. R. Luo, *Sci. Rep.*, 2016, **6**, 32388.
12 Y. Huang, X. Xie, M. Pu, Y. Guo, M. Xu, X. Ma, X. Li and X. Luo, *Adv. Opt. Mater.*, 2020, **8**, 1902061.
13 J. Geng, X.-H. Deng, Z. Xiong, J. Gao, B. Song and J. Yuan, *Chin. J. Phys.*, 2024, **92**, 1312–1324.
14 S. Huang, Y. Chen, C. Yu, S. Chen, Z. Zhou, J. Liang and W. Dai, *Chin. J. Phys.*, 2024, **89**, 740–747.
15 J. C. Wilson, P. Gutsche, S. Herrmann, S. Burger and K. M. McPeak, *Opt. Express*, 2019, **27**, 5097–5115.
16 B. Chen, W. Zhu, H. Jiang, L. Wang, C. Zhou and H. Zhang, *Opt. Lett.*, 2025, **50**, 3321–3324.
17 S. Kim, H. Jang, J. Han, J. Lee and Y. C. Jun, *Nano Lett.*, 2025, **25**, 2841–2849.
18 H. Jiang, K. Peng, Y. Cui, J. Zhong, H. Zhang, Y. Jiang and W. Zhao, *Opt. Lett.*, 2022, **47**, 1907–1910.
19 Z. Yu, M. Li, Z. Xing, H. Gao, Z. Liu, S. Pu, H. Mao, H. Cai, Q. Ma, W. Ren, J. Zhu and C. Zhang, *Opto-Electron. Sci.*, 2024, **3**, 240016.
20 S. Ma, P. Zhang, X. Mi and H. Zhao, *Opt. Commun.*, 2023, **528**, 129021.
21 J. Zeng, Y. Zhou, X. Fu, J. Yang, Y. Chen and W. Hong, *Opt. Express*, 2025, **33**, 27014–27025.
22 Z. Li, R. Yang, J. Wang, Y. Zhao, J. Tian and W. Zhang, *Opt. Mater. Express*, 2021, **11**, 3507–3519.
23 J. Zhang, K. Zhang, A. Cao, Y. Liu and W. Kong, *Opt. Express*, 2020, **28**, 26102–26110.
24 Z. Chen, H. Tang, Z. Chen, T. Shen and H. Zhang, *J. Electron. Mater.*, 2024, **53**, 2676–2685.
25 D. Liu and Z. Cui, *Opt. Mater.*, 2024, **152**, 115478.
26 Y. Wan, T. Sun, Q. Song, Z. Yi, S. Cheng, C. Tang and Y. Yi, *Diamond Relat. Mater.*, 2025, **153**, 112090.
27 G. Wang, X. Zhang, J. Liu, H. Feng, M. Li, S. Yang, Y. Jia, H. Meng and Y. Gao, *Opt. Mater.*, 2024, **150**, 115177.
28 J. Yang, G. Zheng, X. Zha, H. Xi, Z. Yin, J. Zhu and G. Deng, *Opt. Commun.*, 2024, **565**, 130653.
29 Z. Cui, D. Liu, W. Zhu, S. Zhang and L. Wang, *Micro Nanostruct.*, 2024, **186**, 207734.
30 Z. Zheng, C. Gong, H. Zhang, M. Liu, S. Cheng and Z. Yi, *Dalton Trans.*, 2025, **54**, 14132–14141.
31 R. Lai, H. Chen, Z. Zhou, Z. Yi, B. Tang, J. Chen, Y. Yi, C. Tang, J. Zhang and T. Sun, *Micromachines*, 2023, **14**, 1802.
32 Y. Luo, W. He, K. Ren, C. Zhang, L. Zuo, F. Shang, Y. Ding and M. Sun, *Ceram. Int.*, 2025, **51**, 39353–39372.
33 N. Liu, Z. Cui, S. Zhang and L. Wang, *Solid State Commun.*, 2025, **399**, 115884.
34 X. Wang, M. Chen, W. Zhao, X. Shi, W. Han, R. Li, J. Liu, C. Teng, S. Deng, Y. Cheng and L. Yuan, *Opt. Express*, 2023, **31**, 22144–22156.
35 Y. Zhu, Z. Cui, S. Zhang and L. Wang, *Solid State Commun.*, 2025, **404**, 116087.
36 H. Yang, H. Sun, Y. Yang, Q. He, X. Gongli, B. Wang and L. Shao, *Opt. Commun.*, 2024, **559**, 130403.
37 R. T. Ako, W. S. L. Lee, M. Bhaskaran, S. Sriram and W. Withayachumnankul, *APL Photonics*, 2019, **4**, 096104.
38 K. Yi, D. Liu, X. Chen, J. Yang, D. Wei, Y. Liu and D. Wei, *Acc. Chem. Res.*, 2021, **54**, 1011–1022.

39 J. T. Wang, P. Tonkaev, K. Koshelev, F. Lai, S. Kruk, Q. Song, Y. Kivshar and N. C. Panoiu, *Opto-Electron. Adv.*, 2024, **7**, 230186.
40 K. An, M. Liu, H. Yang, Z. Yi, C. Tang, J. Deng, J. Wang and B. Li, *Phys. E*, 2026, **175**, 116377.
41 J. Wang, M. Liu, H. Yang, Z. Yi, C. Tang, J. Deng, J. Wang and B. Li, *Opt. Commun.*, 2025, **596**, 132415.
42 Z. Chen, M. Liu, S. Cheng, J. Wang, Y. Yi, B. Li, C. Tang and F. Gao, *Curr. Appl. Phys.*, 2025, **80**, 282–290.
43 Z. Cui, H. Xu, X. Wang, L. Xia, S. Zhang and L. Wang, *Micro Nanostruct.*, 2026, **212**, 208569.
44 Z. Cui, N. Liu, Y. Zhang and M. Wang, *Opt. Commun.*, 2024, **570**, 130874.
45 S. Wang, N. T. Hung and M. Sun, *Molecules*, 2026, **31**, 215.
46 K. Ren and M. Sun, *J. Appl. Phys.*, 2025, **137**, 130402.
47 Z. Cui, Y. Zhu, Y. Zhang, S. Zhang and L. Wang, *Phys. B*, 2025, **696**, 416641.
48 A. Gulzar, P. Yang, F. He, J. Xu, D. Yang, L. Xu and M. O. Jan, *Chem.-Biol. Interact.*, 2017, **262**, 69–89.
49 G. Li, G. Wang, T. Yang, Y. Zhang, J. Shen and B. Zhang, *Nanoscale Adv.*, 2022, **4**, 3342–3352.
50 J.-J. Luo, Y.-H. Sun, G.-Z. Zhou, H.-X. Li and H.-F. Zhang, *Int. Commun. Heat Mass Transfer*, 2026, **172**, 110356.
51 S. Dai, S. Y. Liao, J. R. Pan and H. F. Zhang, *Nanoscale*, 2025, **17**, 12673–12683.
52 C. Menzel, C. Rockstuhl and F. Lederer, *Phys. Rev. A*, 2010, **82**, 053811.
53 J. Yao, D. Liu and H. Du, *Phys. B*, 2025, **718**, 417908.
54 D. Li, S. He, L. Su, H. Du, Y. Tian, Z. Gao, B. Xie and G. Huang, *Opt. Mater.*, 2024, **147**, 114655.
55 M. Chen, W. Sun, J. Cai, L. Chang and X. Xiao, *Plasmonics*, 2017, **12**, 699–705.
56 H. Zhang, L. Si, T. Ma, L. Dong, R. Niu, X. Bao, H. Sun and J. Ding, *Electronics*, 2022, **11**, 24.
57 C. Rong, B. Cai, Y. Cheng, F. Chen, H. Luo and X. Li, *Phys. Chem. Chem. Phys.*, 2024, **26**, 5579–5588.
58 U. U. R. Qureshi, B. Hu, M. Ahmad and A. Jalal, *IEEE Photonics Technol. Lett.*, 2023, **35**, 1375–1378.
59 X. Wang, M. Chen, W. Zhao, R. Li, X. Shi, W. Han, J. Liu, C. Teng, S. Deng, Y. Cheng and L. Yuan, *Opt. Laser Technol.*, 2024, **170**, 110190.
60 U. U. R. Qureshi, S. Basir, F. Mallek and H. Hamam, *Sci. Rep.*, 2024, **14**, 5118.